



Synthesis of sustainable aviation biofuels via catalytic hydropyrolysis of lignin

Tan Li^{a,b}, Yang Meng^{b,c}, Linjia Yin^a, Bingyan Sun^a, Wanchen Zhu^a, Jing Su^a, Kaige Wang^{a,*}

^a State Key Laboratory of Clean Energy Utilization, Zhejiang University, Hangzhou 310027, PR China

^b Department of Chemistry, National University of Singapore, Singapore 117543, Singapore

^c School of Chemistry and Chemical Engineering, Guizhou University, Guiyang 550025, China

ARTICLE INFO

Keywords:

Catalytic hydropyrolysis
Sustainable aviation biofuel
Hydrodeoxygenation
Lignin
NiMo/SiO₂ catalyst

ABSTRACT

The exploitation of bimetallic catalysts to lignin for sustainable aviation biofuels remains a daunting challenge due to the low selectivity of aviation biofuel-range hydrocarbons and inconsistent reaction mechanism. Herein, bimetallic supported on SiO₂ catalysts were prepared and their hydrodeoxygenation reactivity during lignin catalytic hydropyrolysis was explored. Approximately 100 % selectivity toward aviation-range hydrocarbons were achieved using eugenol as model compound under relatively mild conditions with the presence of NiMo/SiO₂. For lignin catalytic hydropyrolysis, the yield of liquid hydrocarbons and the selectivity of aviation-range hydrocarbons was 21.99 wt% and 70.50 %, respectively. High mass balance (89.66 %) was verified by scale-up experiments in a continuous flow high-pressure reactor system. The reactivity of demethoxylation reaction, dehydroxylation reaction, and benzene ring hydrogenation reaction with the presence of bimetallic catalysts were analyzed. The density functional theory calculation and verification experiments revealed the evolution pathway of aromatic hydrocarbons and cycloalkanes from lignin catalytic hydropyrolysis. The proposed reaction mechanism can provide guidance for the regulation of aviation biofuel components from lignin catalytic hydropyrolysis.

1. Introduction

Aviation fuel, which contains 30–70 % aromatics and cycloalkanes, has shown an increasing supply gap with the progress of human society [1]. In 2022, 2.3 billion gallons of kerosene-type aviation fuel were consumed in U.S. [2]. It is forecasted that U.S. aviation fuel demand will increase by 6 % in 2024 [3]. Meanwhile, to mitigate the climate impact of overuse of aviation fuel, the aviation industry has promised to realize net carbon neutrality by 2025 [1]. Lignin, which has been considered as a byproduct in many biorefinery processes [4], is the largest renewable resource of aromatic building blocks in nature. The unique structure and massive sources make lignin a potential feedstock to produce aviation biofuel.

Hydrodeoxygenation reaction can convert lignin and its derivatives to aromatics and cycloalkanes with the presence of hydrogen and heterogeneous catalysts [5,6]. A lot of efforts have been made to design a heterogeneous catalyst, presenting high hydrodeoxygenation activity and weak alkyl branch chain breaking ability [7,8], which can enhance the formation of aviation fuel-range aromatics and cycloalkanes.

Conventional Mo-based catalysts were often used to catalyze lignin conversion to produce biofuel [9]. However, the weak hydrogen dissociation ability of these catalysts made the yield of liquid hydrocarbon products low. Bimetal supported catalysts, with metal A to enhance hydrogenation reaction and metal B to promote deoxygenation reaction, has the potential to enrich liquid hydrocarbon products during lignin hydrodeoxygenation. Metal A usually includes noble metals like Pt, Pd, Ru [10–14], and non-noble metals like Ni, Fe, Co [6,15–19]. Metal B usually contains non-noble metals like W and Mo [20,21]. Noble metal catalysts can greatly facilitate the dissociation of hydrogen, the activation of C–O bond, and C–C bond by electronic charge redistribution, which facilitates the formation of cycloalcohols [22,23]. Non-noble metal catalysts show great potential in the field of lignin hydrodeoxygenation due to their low price and optimizable activity. Ha et al. introduced Fe onto Ni/TiO₂ to construct the interface site of the highly dispersed NiFe-FeO_x core-shell structure, which resulted in the highly selective formation of cyclohexanol (selectivity: 85 %) by direct demethoxylation and hydrogenation of guaiacol [15]. Without the presence of metals with deoxygenation reaction activity, the C_{ar}–O bond on

* Corresponding author.

E-mail address: kaigewang@zju.edu.cn (K. Wang).

<https://doi.org/10.1016/j.apcatb.2024.124092>

Received 23 December 2023; Received in revised form 7 April 2024; Accepted 17 April 2024

Available online 18 April 2024

0926-3373/© 2024 Elsevier B.V. All rights reserved.

phenolic compounds is difficult to be removed. Li et al. first synthesized NiMoO_4 through hydrothermal method and then prepared Ni-MoO_{3-x} catalyst by low temperature reduction, which resulted in numerous oxygen vacancies around the nickel clusters [24]. In the hydrodeoxygenation experiment of cresol, Ni-MoO_{3-x} showed high activity at 150 °C with a selectivity of 99.4 % for methylcyclohexane. Resasco et al. introduced W onto Ni/SiO_2 , which not only made the hydrodeoxygenation reaction rate of m-cresol increase by nearly one order of magnitude at 350 °C and 1 atm H_2 , but also significantly reduced the CH_4 yield [25]. The formation of NiW alloy led to a significant reduction in the chemisorption of CO, which provided balanced hydrogenation, oxophilicity, and C–O cleavage activity. Above facts indicates that a reasonable matching of non-noble metal can achieve complete deoxygenation and the retention of alkyl branch chains.

In addition, there are still different views on the hydrodeoxygenation mechanism of lignin under the action of hydrogen and bimetal supported catalysts, especially the formation mechanism of cycloalkanes and aromatic hydrocarbons [26–29]. Ma et al. found the effect of different carriers on the mechanism of hydrodeoxygenation of phenolic compounds [30]. In the hydrodeoxygenation experiments of phenol, the hydrogenation of aromatic ring was occurred preferentially on Ni/SiO_2 catalyst, while the hydrocrack reaction of $\text{C}_{\text{ar}}\text{--O}$ bond was preferentially happened on $\text{Ni}/\gamma\text{-Al}_2\text{O}_3$ catalyst. Lin et al. introduced a second metal into Ni/SiO_2 to improve the catalyst's oxophilicity [31]. The results showed that the hydrogenation reaction of p-cresol occurred preferentially in hydrogen atmosphere, and then the phenol hydroxyl was removed to form methylcyclohexane. Although numerous DFT calculations and experiments have been performed [32–34], there are still a lot of different views about hydrodeoxygenation mechanism of lignin. Zhang et al. used $\text{Ni}/\text{HZSM-5}$ to investigate the hydrodeoxygenation mechanism of monophenol to produce monoaromatics [35]. The results revealed that the acid site promoted the initial tautomerism reaction and the final dehydration reaction of phenols, while Ni enhanced the hydrogenation reaction of intermediates, which realize the direct hydrodeoxygenation of phenol to produce benzene with high selectivity. Creaser et al. observed a similar phenomenon [36], in which the removal of phenolic hydroxyl groups preceded the hydrogenation of benzene ring structure. Inspired by the above facts, designing a bimetallic catalyst with a reasonable combination of bimetallic sites should be a promising strategy for synergistically catalyzing lignin to achieve high yield of aviation-range hydrocarbons. Nonetheless, given the complex pathways of lignin depolymerization and the difficulty in monitoring the catalysis process, it is a challenging task to reveal the formation mechanism of aviation biofuel range components.

Herein, bimetallic supported SiO_2 catalysts were used in the catalytic hydropyrolysis of lignin and its derivatives. The influence of variables such as reaction temperature, reaction pressure, and reaction time on the product distribution was discussed. The physical and chemical properties of the catalysts were characterized in detail. NiMo showed the most balanced reactivity of methoxy group removal reaction, phenol hydroxyl group removal reaction, and benzene ring hydrogenation reaction. Density functional theory (DFT) calculations and experiments revealed the evolution pathway of aromatic hydrocarbons and cycloalkanes from lignin catalytic hydropyrolysis, which may serve as a guidance for regulating the proportion of aromatic hydrocarbons in sustainable aviation biofuels.

2. Experimental

2.1. Chemicals

Milled wood lignin (MWL) extracted from Chinese fir was prepared using the method described in previous studies [37,38]. The enzymolysis lignin obtained by hydrolyzing corn cob with dilute sulfuric acid and cellulose complex enzyme was derived from Sinopec Group. Eugenol (AR, 99.5 %, Aladdin), ethylphenol (AR, 95 %, Macklin), and

ethylguaicol (AR, 99 %, Aladdin) were used as feedstocks. Acetone (AR, 99 %, Sinopharm Chemical Reagent Co., Ltd.) and naphthalene (AR, 99.5 %, Macklin) were used as solvent and internal standard, respectively. Silica (Tsingtao sea chemical incorporated company), nickel nitrate hexahydrate (AR, 98 %, Alfa Aesar), cobalt nitrate hexahydrate (AR, 99 %, Aladdin), ammonium molybdate tetrahydrate (AR, 99 %, Macklin), ammonium metatungstate (AR, 98.5 %, Rhwan), and ammonium hydroxide (AR, 25–28 %, Sinopharm Chemical Reagent Co., Ltd.) were used for catalyst preparation.

2.2. Catalyst preparation

The catalysts were prepared by coprecipitation method. Take NiMo/SiO_2 as an example to describe a typical preparation process. The loading of Ni and Mo were 10 wt% and 5 wt%, respectively. The calculated amount of nickel nitrate hexahydrate was dissolved in 50 mL of deionized water. The calculated amount of SiO_2 was added to the above solution and vigorously stirred at room temperature for 6 h. Ammonium hydroxide was then added drop by drop to the mixture to maintain a pH of 8–10. The mixture was stirred at room temperature for 12 h. The sediment was filtered out and washed three times with deionized water. The prepared catalyst was dried overnight at 105 °C and then calcined at 500 °C for 4 h. Before the experiment, the catalyst was reduced under H_2 flow (50 mL/min) at 500 °C (5 °C/min ramping rate) for 4 h and passivated under 1 % O_2/N_2 (40 mL/min) for 0.5 h. For NiW/SiO_2 (The loading of Ni and W were 10 wt% and 5 wt%, respectively) and CoMo/SiO_2 (The loading of Co and Mo were 10 wt% and 5 wt %, respectively), the metal precursor will be replaced with the corresponding metal salt respectively.

2.3. Catalyst characterizations

The specific surface area and pore distribution of the catalysts were measured by a Micromeritics ASAP 2460 instrument. The specific surface area and pore size distribution were calculated by the Brunner-Emmet-Teller (BET) method and the Barret-Joyner-Halenda (BJH) method, respectively. The X-ray diffraction (XRD) patterns of the catalysts were analyzed by an X-ray powder diffractometer (Smartlab 9kw, Rigaku) with a 2-theta range of 10–90° and a scanning rate of 5°/min. The X-ray photoelectron spectroscopy (XPS) analysis of the catalysts was conducted on a Thermo Scientific K-Alpha with Al K α monochromatic radiation ($h\nu$, 1486.6 eV). A FEI Tecnai F20 transmission electron microscope (TEM) equipped with an X-ray energy spectrum analyzer (EDS) was used for the morphology analysis of catalysts. The accelerating voltage is 120 kV. Hydrogen temperature-programmed reduction (H_2 -TPR) and temperature-programmed desorption of ammonia (NH_3 -TPD) analysis were conducted on a chemisorption instrument (BelCata II, Japan). Pyridine infrared spectroscopy (Py-IR) tests were performed on a Fourier transform infrared spectrometer (Bruker Tensor 27). The actual loading of the various metals in the three catalysts were tested by Inductively Coupled Plasma-Optical Emission Spectrometer (ICP-OES, Agilent 5100). Detailed information about catalyst characterizations was shown in [Supporting Information](#).

2.4. Catalytic performance test and product analysis

The catalytic experiments of lignin model compounds were carried out in a 50 mL stainless steel autoclave reactor. 10 mmol substrate and 0.1 g pre-reduced catalyst were loaded in the reactor. After sealing, the reactor was purged with nitrogen three times to remove the air in the reactor. The reactor was then pressurized with hydrogen. The reaction was carried out under agitation. All experiments were performed three times. After the reaction was completed, 5 mL of acetone was added to dissolve the products and 1 mmol naphthalene was added as the internal standard. The liquid products were quantified by a gas chromatograph (GC) and a mass spectrometer (MS) system (GC: Agilent 8860, MSD:

Agilent 5977B) with an DB-1701 column using internal standard method. The oven temperature was kept constant at 40 °C for 3 min, then raised to 250 °C at a rate of 5 °C/min, after which temperature was held constant for 8 min.

The catalytic hydrolysis experiments of MWL were conducted in a high pressure tandem micro-pyrolyzer (Py: Rx-3050 TR, Frontier Laboratories, Japan) combined with a GC/MS system (GC: Agilent 7890B, MS: 5977B). A detailed description of this system can be found in our previous research [39,40]. For a typical experiment, 1 mg feedstock and 4 mg catalyst were loaded in the 1st reactor and 2nd reactor, respectively. Hydrogen (56 mL/min) was used as the reaction gas and the carrier gas. The pyrolysis products were analyzed on-line by the GC/MS equipped with a flame ion detector (FID) and a thermal conductivity detector (TCD). The GC oven was programmed for an 8 min held at 30 °C then ramped at 5 °C/min to 250 °C, after which temperature was held constant for 4 min. The mass yield of char was calculated by weighing the mass of the sample cup before and after the reaction by using a microbalance (XPR10, Mettler Toledo, Switzerland).

The scale-up experiment was carried out in a continuous flow high-pressure reactor system, scheme of which was shown in Fig. S1. The enzymolysis lignin (40–80 mesh) was fed to the free-fall pyrolysis reactor by an auger. Pyrolysis vapor was carried to the downstream catalysis region which was filled with NiMo/SiO₂ (20 g, 40–80 mesh) diluted with passivated quartz sand (20 g, 40–80 mesh). The temperature in the pyrolysis zone and catalytic zone were set at 500 °C and 350 °C, respectively. The hydrogen pressure in the system was maintained 1.0 MPa. The volatile product was condensed and collected by a first-

stage water-cooled collector and a second-stage liquid-nitrogen-cooled collector. The yield of liquid products was determined by weighing, and the specific product distribution was quantified by GC/MS as mentioned earlier. Pyrolysis char fell into the char collector and weighed to determine its yield. The gas products were collected by air bag and quantified by GC-TCD (GC: Agilent 8860).

2.5. Quantum chemistry calculation

All calculations were carried out using the Gaussian 03 suite of programs (Gaussian Inc., USA) [41]. The molecular structures of modeling compounds were optimized using the density functional theory (DFT) methods employing B3LYP/6-31G(d). Based on the results obtained from Gaussian calculations, the BO and f(0) based on free radical attack were derived using Multiwfn [42].

All energy and charge calculations were performed by using the Vienna Ab-initio Simulation Package (VASP) software [43,44]. The projector augmented wave (PAW) potential and generalized gradient approximation with Perdew–Burke–Ernzerh (GGA-PBE) functional was used to describe the exchange–correlation interactions. The van der Waals (vdW) correction DFT-D3 proposed by Grimme was chosen due to the good description of long-range vdW interactions. Moreover, the plane wave cutoff energy was set to be 520 eV, and $1 \times 1 \times 1$ k-points was applied to the sample Brillouin zone for $4 \times 4 \times 1$ super cells. 15 Å vacuum space was used to avoid the layers' interactions. The electronic energy was considered self-consistent when the energy change was smaller than 10^{-5} eV. Geometry optimization was considered

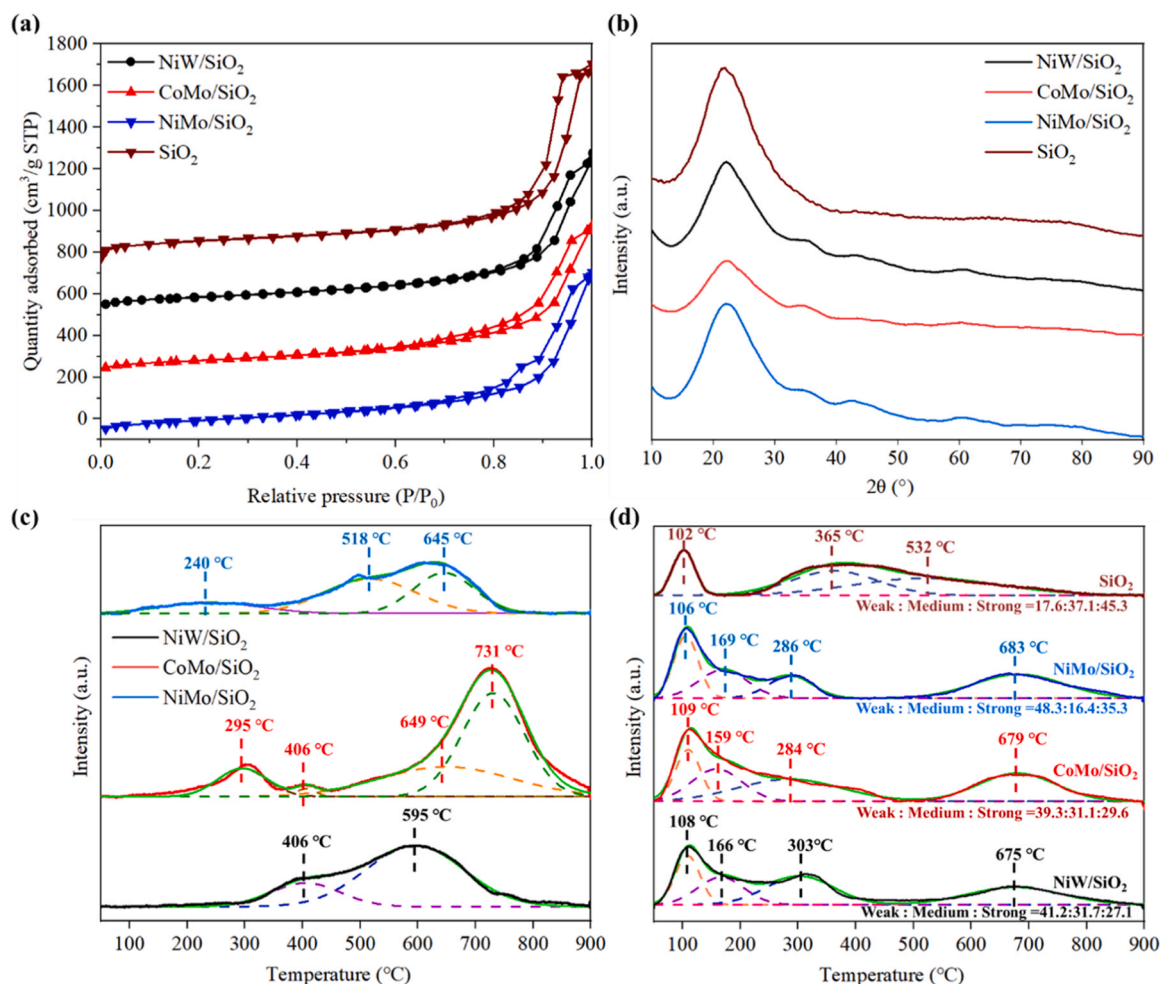


Fig. 1. (a) N₂ adsorption-desorption isotherms, (b) XRD patterns, (c) H₂-TPR profiles, and (d) NH₃-TPD profiles of NiW/SiO₂, CoMo/SiO₂, NiMo/SiO₂, and SiO₂.

convergent when the energy was smaller than 0.02 eV/Å. The Dimer method was used to search for the transition state.

3. Results and discussion

3.1. Characterization of catalysts

The nitrogen adsorption and desorption curves of four catalysts were type IV with H1 hysteresis loops, as shown in Fig. 1a, which indicated the uniform cylindrical mesoporous structure of the catalysts. The textural properties of the catalysts are summarized in Table 1. The loading of bimetal made the specific surface area, pore volume and average pore size of SiO₂ carrier slightly decreased, which is due to the blockage of the catalyst channel. Compared with other bimetallic doped SiO₂, NiMo/SiO₂ exhibited the largest specific surface area (324.41 m²/g) and pore volume (1.16 cm³/g). By replacing Ni with Co, the specific surface area and pore volume of the catalyst decreased to 285.76 m²/g and 1.06 cm³/g, respectively. Compared with NiMo/SiO₂, NiW/SiO₂ also showed smaller specific surface area (295.54 m²/g) and pore volume (1.12 cm³/g). The average pore sizes and mesopores of bimetallic doped SiO₂ catalysts were concentrated in the range of 14–16 nm and 86–93 % respectively, which further indicated that they have uniform mesoporous structures.

The XRD pattern of all catalysts only showed a broad and gentle peak belonging to SiO₂ (#PDF 27-0605) (Fig. 1b), indicating that SiO₂ is in an amorphous state. As shown in Table S1, the actual loading of metal in the three catalysts was slightly lower than the theoretical loading. It is inferred that the absence of obvious peak of loaded metal might result from the fact that amorphous materials have more lattice defects than crystalline materials, which helps to improve the dispersion of loaded metals [45].

The H₂-TPR profiles of bimetallic supported on SiO₂ catalysts are shown in Fig. 1c. For NiMo/SiO₂, the first peak at 240 °C represented the reduction from Ni²⁺ species to Ni⁰ species [46]. The second peak at 518 °C represented the reduction of the polyoctahedral Mo⁶⁺ species to Mo⁴⁺ species [47]. The third peak at 645 °C represented the reduction from Mo⁴⁺ species to Mo⁰ species [47]. At a reduction temperature of 500 °C, NiMo/SiO₂ contained mainly Ni⁰ species and Mo⁴⁺ species. For CoMo/SiO₂, the four peaks were successively Co₃O₄ to CoO, CoO to Co⁰, Mo⁶⁺ to Mo⁴⁺, and Mo⁴⁺ to Mo⁰, respectively [48]. Compared with NiMo/SiO₂, the reduction peak of Mo species in CoMo/SiO₂ appeared at a higher temperature, which indicated that Mo species in CoMo/SiO₂ had a strong interaction with SiO₂. For NiW/SiO₂, the two peaks were successively NiO to Ni, and the octahedral coordination polymer tungsten species to the low coordination tungsten species [49]. Compared with NiMo/SiO₂, the reduction peak of Ni species in NiW/SiO₂ appeared at a higher temperature (406 °C), which showed that Ni species in NiW/SiO₂ had a stronger interaction with SiO₂. Too strong interaction between highly dispersed active metals and the support may result in passivation of the active site [50].

The acidity of the catalysts is very important for the removal of the oxygen-containing functional groups. Py-IR results were used to identify

the acid site types of the catalysts, as shown in Table 1 and Fig. S2. The strong bands at 1448 and 1542 cm⁻¹ belonged to the Lewis acid site and Brønsted acid site, respectively. All bimetallic doped catalysts were dominated by Lewis acid sites. It is due to the fact that the metal oxides evenly distributed on the surface of SiO₂ can act as extra Lewis acid sites, which is consistent with the results of NH₃-TPD. NiW/SiO₂ had the highest proportion of Lewis acid sites (91.82 %). When changed W to Mo, the proportion of Lewis acid sites slightly decreased to 88.25 %. Both MoO_x species and WO_x species could act as Lewis acid sites, so there is no significant change in the proportion of Lewis acid sites.

The NH₃-TPD results of four catalysts are shown in Fig. 1d and Table 1. The increasing order of the acidity of the catalysts was SiO₂ (1.46 mmol/g) < NiMo/SiO₂ (1.71 mmol/g) < CoMo/SiO₂ (1.73 mmol/g) < NiW/SiO₂ (2.51 mmol/g). The loading of bimetal made the acidity of SiO₂ increased, which is due to the fact that high valence metals can act as Lewis acidic sites. The NH₃-TPD curves of all catalysts after deconvolution contained four distinct peaks, and the proportion of weak acidic sites (100–200 °C) was higher than that of medium acidic sites (200–450 °C) and strong acidic sites (temperature greater than 450 °C). For SiO₂, the strong acidic sites (45.3 %) dominated the acidic sites. The introduction of metals increased the proportion of weak acidic sites at the expense of strong and medium acidic sites. Among the bimetal doped SiO₂, NiMo/SiO₂ showed the largest proportion of weak acidic sites (48.3 %). When Ni was replaced with Co, the proportion of medium acidic sites increased from 16.4 % to 31.1 % at the expense of weak acidic and strong acidic sites. When Mo was replaced by W, the proportion of weak acidic sites also showed a downward trend. Combined with Py-IR results, the reasonable matching of Ni and Mo resulted in the highest proportion of weak Lewis acidic sites on NiMo/SiO₂ catalyst, which will inhibit the formation of coke during the phenolic conversion process [51,52]. The presence of weak Lewis acidic sites in catalysts is also correlated with the deoxidation rate in the hydrodeoxygenation reaction. The increased abundance of weak Lewis acidic sites may decrease the activation energy of the HDO reaction [53–55].

XPS spectra of bimetallic supported on SiO₂ catalysts are summarized in Fig. 2. As shown in Fig. 2a, the deconvolution of the Ni 2p spectra proved the presence of Ni²⁺ species at 856.0 eV and 873.8 eV. Two obvious satellite peaks of NiO were also detected at 861.8 eV and 881.8 eV, which proved the presence of Ni species. Four obvious peaks at 229.1 eV, 234.2 eV, 232.1 eV, and 236.7 eV in Fig. 2b were contributed to Mo⁴⁺ species and Mo⁶⁺ species, which meant that polyvalent Mo species exist on both NiMo/SiO₂ and CoMo/SiO₂. The peaks at 781.3 eV and 797.1 eV were related to Co³⁺ species (Fig. 2c), which indicated the presence of Co species on the surface of CoMo/SiO₂. As shown in Fig. 2e, the peaks at 34.9 eV and 37.4 eV were associated with W⁶⁺ species. Ni or Co doped catalysts may undergo violent oxidation when exposed to air directly after reduction. To avoid violent oxidation, all catalysts have been passivated in 1 % O₂/N₂ atmosphere for 0.5 h after reduction, which resulted in the formation of NiO_x and CoO_x on the surface of these catalysts. In the actual catalytic conversion experiments under high pressure hydrogen atmosphere, a large number of the low-valence state Ni or Co species inside the catalyst, which is proved by H₂-TPR results,

Table 1
Textural properties of four catalysts.

Sample	S _{Bet} ^a (m ² /g)	V _{total} ^b (cm ³ /g)	Pore size ^c (nm)	Mesopores (%)	Total acidity (mmol/g) ^d	Brønsted acid (%) ^e	Lewis acid (%) ^e
SiO ₂	359.00	1.37	19.60	92.93	1.46	-	-
CoMo/SiO ₂	285.76	1.06	14.01	87.39	1.73	15.42	84.58
NiW/SiO ₂	295.54	1.12	15.23	92.63	2.51	8.18	91.82
NiMo/SiO ₂	324.41	1.16	14.59	86.85	1.71	11.75	88.25

^a Specific surface area is calculated from the adsorption branch of the N₂ isotherm.

^b Total pore volumes are calculated from the N₂ adsorption isotherm at a relative pressure of 0.99.

^c Mesopore diameter is calculated from the adsorption branch using the BJH method.

^d The catalysts are reduced *in-situ* before testing.

^e Acid sites after desorption at 350 °C.

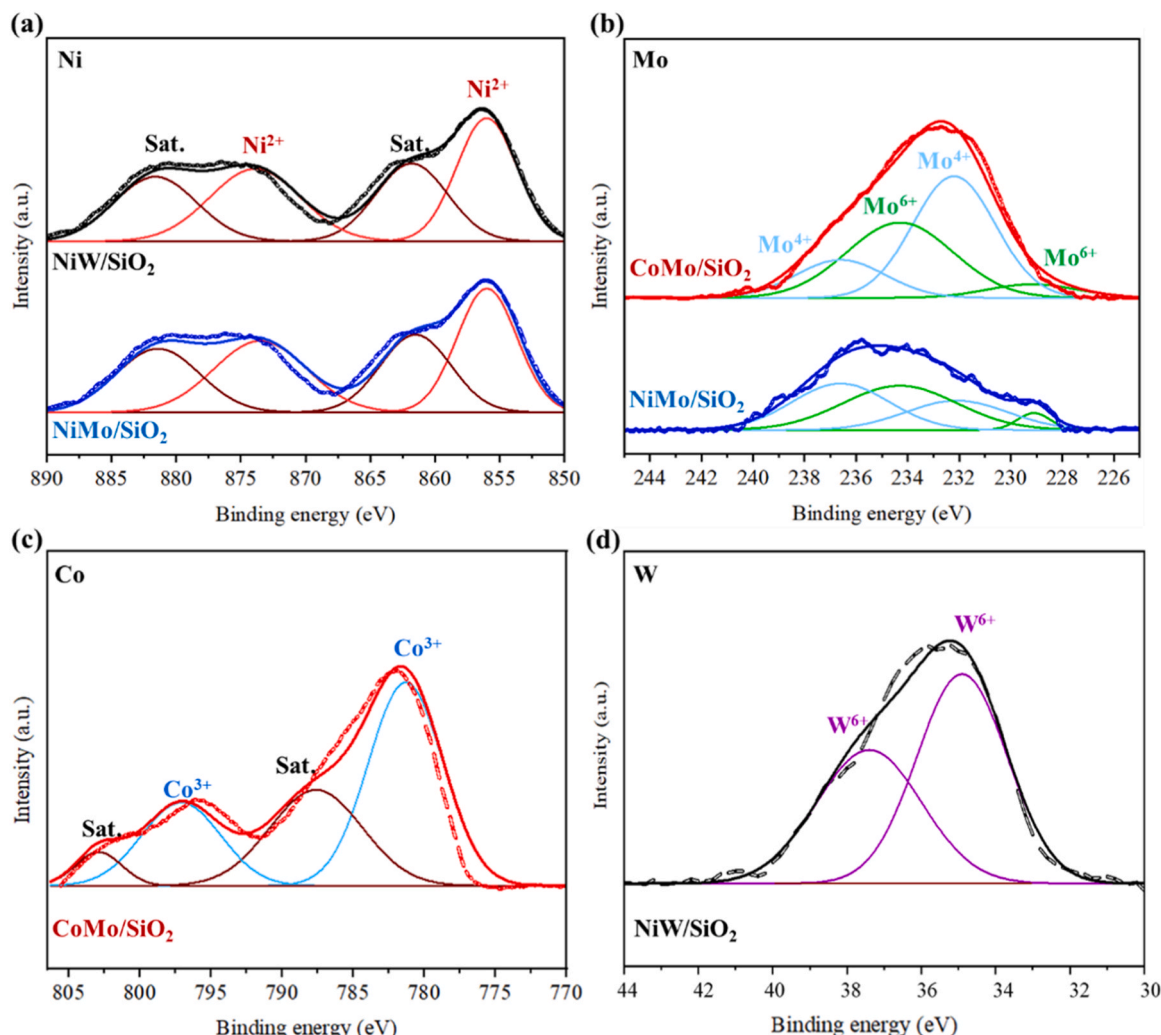


Fig. 2. XPS spectra of NiW/SiO₂, CoMo/SiO₂, and NiMo/SiO₂ in the ranges of (a) Ni 2p, (b) Mo 3d, (c) Co 2p, and (d) W 4f.

will act as the primary catalytic site.

The morphology and structure of NiMo/SiO₂ are shown in Fig. 3. It can be seen from Fig. 3a that many small active metal particles were attached on the surface of SiO₂. The average particle size of the active metal was 3.05 ± 0.17 nm. Fig. 3b is the SEI image of NiMo/SiO₂, in which the whole catalyst had a coral-like structure. From Fig. 3c, the TEM dark field image, fine active metal particles could be observed. Fig. 3d-f showed the EDS image of NiMo/SiO₂, corresponding to Mo, Ni and Si elements respectively. As shown in Fig. 3d-f, Mo and Ni were uniformly dispersed on the surface of SiO₂, and there was no obvious agglomeration of metal particles.

3.2. Catalyst performance

3.2.1. Screening catalysts

The screening experiments of the catalysts were conducted in a stainless steel autoclave reactor. The results are shown in Fig. 4. The conversion rate of eugenol was 100 % in all experiments. The combination of different active metals has a great influence on the hydrodeoxygenation activity of the catalyst, as shown in Fig. 4. The increasing order of the selectivity of liquid hydrocarbon products with catalysts was CoMo/SiO₂ (40.49 %) < NiW/SiO₂ (47.64 %) < NiMo/SiO₂ (91.63 %), which was consistent with the increasing order of the yield of aviation-range hydrocarbons. In addition, the selectivity of liquid hydrocarbon products increased in the same order as the proportion of

weak Lewis acidic sites in the catalysts. The NiMo/SiO₂ catalyst, with the highest percentage of weak Lewis acidic sites, demonstrated the best hydrodeoxygenation activity, achieving the highest liquid hydrocarbon selectivity (91.63 %) and aviation-range hydrocarbons yield (58.25 wt %). For CoMo/SiO₂ and NiW/SiO₂, products containing both hydroxyl and methoxy groups dominated the liquid products, with a selectivity of 45.92 % and 35.17 %, respectively. With the presence of NiMo/SiO₂, the cycloalcohols (7.75 %) was the main oxygen-containing product in the liquid products.

3.2.2. Screening reaction conditions

The screening experiments of reaction conditions were conducted in a stainless steel autoclave reactor. The results are shown in Fig. 5. At 1.0 MPa H₂, the products containing hydroxyl group (31.28 %) dominated the oxygen-containing liquid products (Fig. 5a). With the increase of hydrogen pressure, the selectivity of liquid hydrocarbon products increased sharply, which was consistent with the increasing trend of selectivity of sustainable aviation biofuels. At 2.0 MPa H₂ and 3 MPa H₂, the hydrocarbon selectivity was close to 100 %, and the yield of aviation-range hydrocarbons was close to 57 wt%. As shown in Fig. 5b, the increasing order of the selectivity of liquid hydrocarbon products with reaction temperature was 220 °C (13.11 %) < 240 °C (91.63 %) < 260 °C (99.76 %). The increase of reaction temperature greatly promoted the selectivity of liquid hydrocarbon products. When the temperature increased from 240 °C to 260 °C, the yield of aviation-range

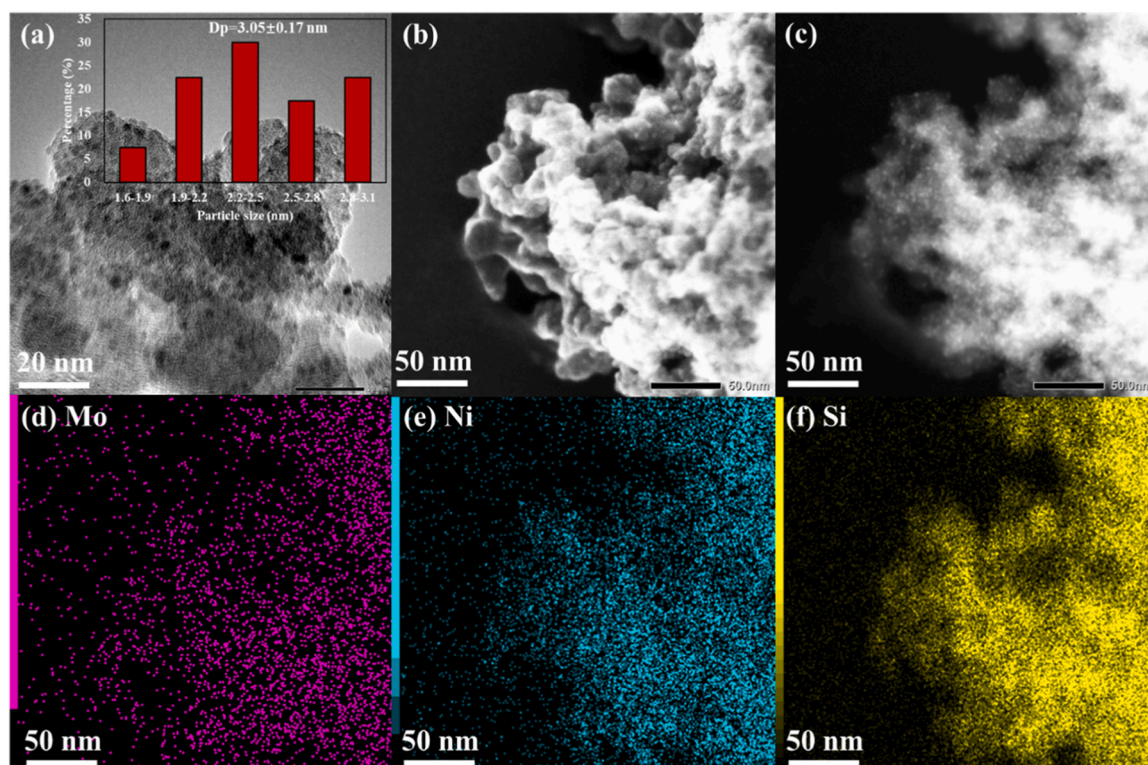


Fig. 3. (a) TEM bright field image of NiMo/SiO₂, (b) SEI image of NiMo/SiO₂, (c) TEM dark field image of NiMo/SiO₂, and (d–f) EDS elemental mapping images of NiMo/SiO₂.

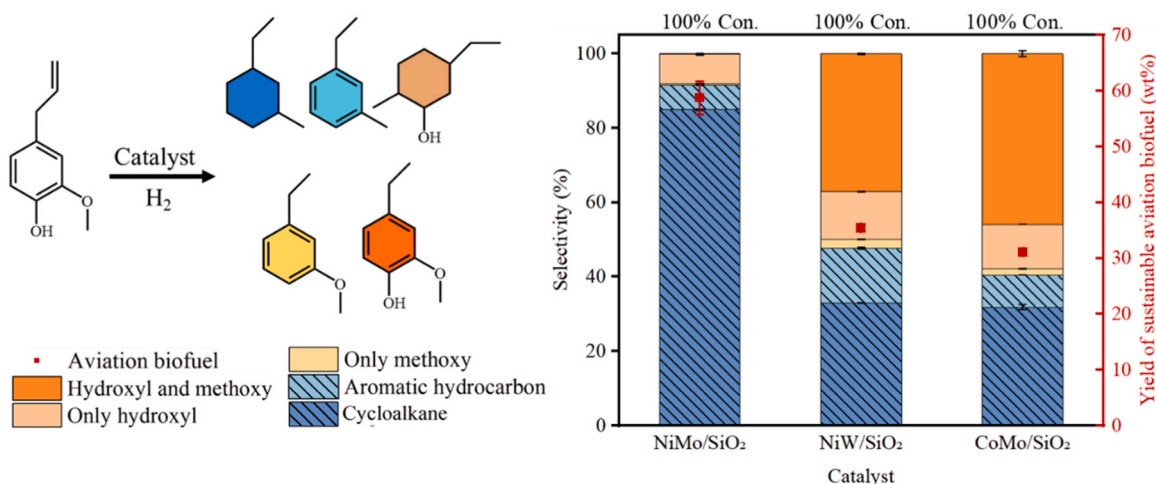


Fig. 4. Variation of liquid product selectivity with of NiW/SiO₂, CoMo/SiO₂, and NiMo/SiO₂. (2 MPa H₂, 4 h, 240 °C, 10 mmol eugenol, 0.1 g catalyst.).

hydrocarbons decreased from 58.25 wt% to 56.21 wt%. The excessively high reaction temperature promoted the hydrocracking reaction, which enhanced the formation of non-aviation biofuel components, mainly cyclohexane (C₆H₁₂) and cyclohexane, methyl- (C₇H₁₄). As shown in Fig. 5c, the increasing order of the selectivity of hydrocarbon products with reaction time was 2 h (85.78 %) < 4 h (99.76 %) < 6 h (100 %). With the extension of reaction time, the selectivity of liquid hydrocarbon products and sustainable aviation biofuels increased significantly, from 87.85 % and 85.67 % at 2 h to 100 % and 99.68 % at 6 h, respectively. The extension of the reaction time made the hydrogen and the reaction intermediate fully contact, which not only improved the utilization rate of hydrogen but also enhanced the hydrodeoxygenation reaction.

The detailed liquid products of catalytic experiments of the three

feedstocks are shown in Table S2-4. As shown in Fig. 5d, the selectivity of liquid hydrocarbon products in all experiments was close to 100 %. The increasing order of the yield of aviation-range hydrocarbons with feedstocks was ethylphenol (48.34 wt%) < ethylguaiaicol (55.18 wt%) < eugenol (56.21 wt%). The increasing order of selectivity of aviation-range hydrocarbons with feedstock was ethylphenol (84.58 %) < ethylguaiaicol (97.09 %) < eugenol (99.53 %). For the catalytic experiment of ethylphenol, the strong hydrocracking ability of NiMo/SiO₂ resulted in a low selectivity of aviation-range hydrocarbons (84.58 %). Cyclohexane, methyl- (C₇H₁₄) was the major non-aviation biofuel component in liquid products.

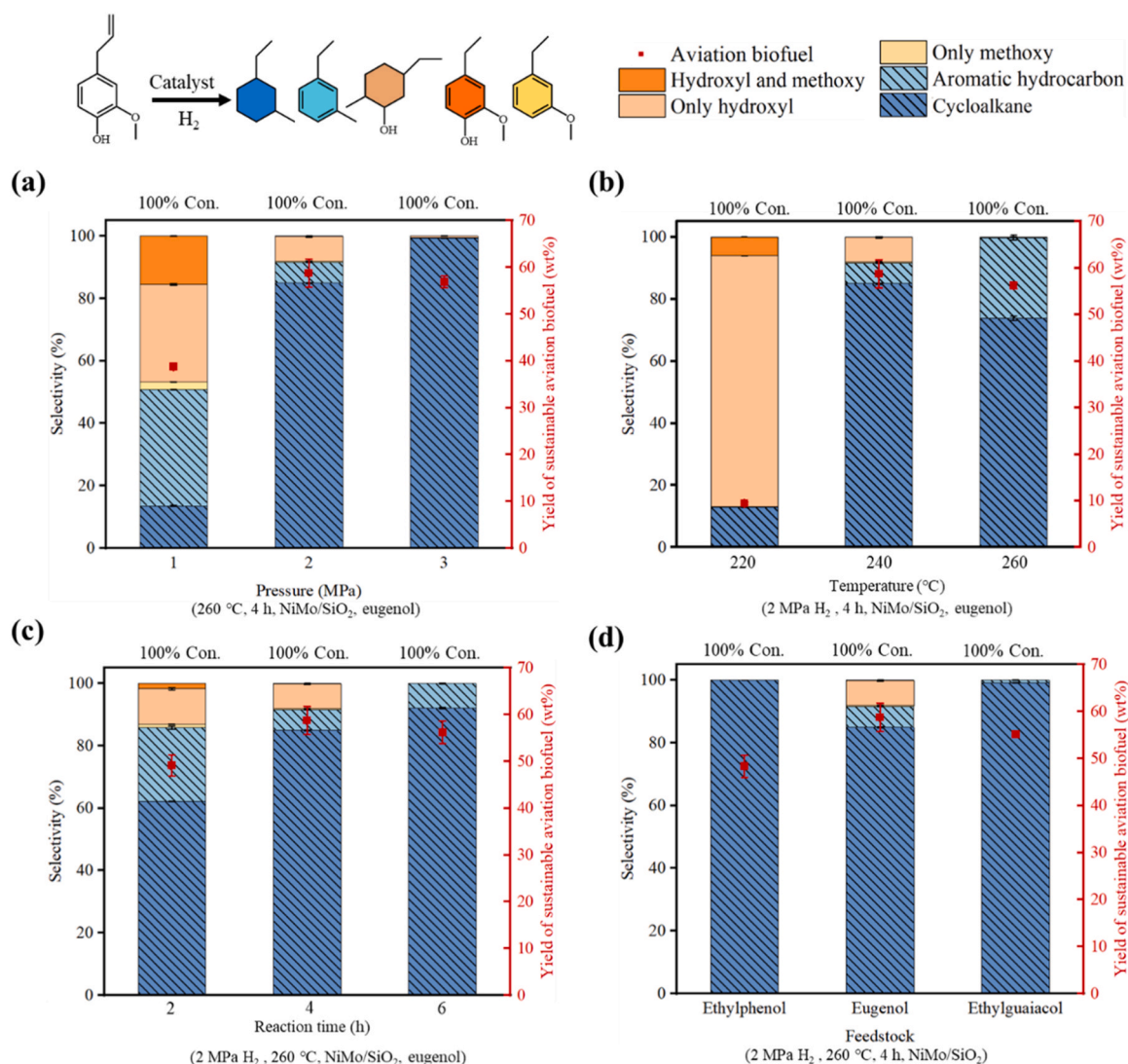


Fig. 5. Variation of liquid product selectivity with the (a) reaction pressure, (b) reaction temperature, (c) reaction time, and (d) feedstock. (10 mmol feedstock, 0.1 g catalyst.).

3.2.3. Production of sustainable aviation biofuels by lignin catalytic hydropyrolysis

The catalytic hydropyrolysis experiments of MWL were carried out in a Py-GC/MS system. As shown in Table 2, the mass balance of three consecutive experiments was close to 61 %, which indicated that the experiments have good repeatability. The formation of heavy components with boiling point higher than 300 °C and water, which cannot be detected by GC/MS, resulted in the relatively low mass balance[56]. The average yield of liquid products was 21.99 wt%, and the average selectivity of aviation-range hydrocarbons was 70.50 %. All the liquid products were cycloalkanes, indicating that the catalyst has good benzene ring hydrogenation reactivity and the hydrodeoxygenation reactivity. It is worth noting that the polycyclic cycloalkanes were detected in the catalytic conversion experiment of MWL (Table 2). The formation mechanism of polycyclic cycloalkanes was verified by the catalytic conversion results of cyclohexanone and cyclohexanol, as shown in Table S5 and Table S6. When cyclohexanone or cyclohexanol was used as feedstock, the formation of polymerization products was detected. When cyclohexanone was used, the polymerization product selectivity (9.68 %) was higher than that of cyclohexanol (3.41 %). Cyclohexanol can produce cyclohexanone by dehydrogenation reaction. Cyclohexanone can further generate polycyclic cycloalkanes by aldol condensation and hydrodeoxygenation reaction[57]. The non-condensable products

of MWL catalytic hydropyrolysis mainly included CH₄, CO, CO₂, and C₃H₈, with average yields of 9.80 wt%, 1.79 wt%, 1.92 wt%, and 0.96 wt%, respectively. CO and CO₂ indicated that some oxygen atom in MWL was removed in the form of decarbonylation and decarboxylation reaction. CH₄ was mainly derived from the breaking of alkyl branch chains[58].

As shown in Table S9, the low-cost NiMo/SiO₂ bimetallic catalyst exhibited excellent HDO activity similar to noble metal doped catalysts for conversion of lignin and its derivatives to aviation biofuels. For catalytic hydropyrolysis of lignin under mild reaction condition, NiMo/SiO₂ showed a higher yield of aviation biofuel than other reported catalysts, which improved the atomic utilization of the process. To further demonstrate the application potential of the catalyst, a laboratory-scale continuous flow experiment was carried out. The results of elemental analysis, industrial analysis and calorific value analysis of enzymolysis lignin used in the scale-up experiment are shown in Table S2. After continuous injection of 12.86 g enzymolysis lignin, the liquid product yield was 36.7 wt% with 7.01 wt% oil phase product. As shown in Table S11, cycloalkanes (56.83 %) and aromatic hydrocarbon (42.08 %) were the main products of oil phase products. The yields of gas products, char, and coke were 19.96 wt%, 30.71 wt%, and 2.59 wt%, respectively. The mass balance of the scale-up experiment was as high as 89.66 %.

Table 2

Yield of various products obtained from catalytic hydroxyprolysis experiments of MWL over NiMo/SiO₂ catalyst. (Reaction condition: 2 MPa H₂, pyrolysis temperature 500 °C, catalytic temperature 300 °C, 1 mg MWL, 4 mg NiMo/SiO₂).

Product	Molecular formula	Run 1	Run 2	Run 3
Monocyclic cycloalkanes (wt %)		17.04	17.62	16.97
Cyclohexane	C ₆ H ₁₂	1.99	2.01	1.87
Cyclohexane, methyl-	C ₇ H ₁₄	4.44	4.59	4.56
Cyclohexane, 1,4-dimethyl-	C ₈ H ₁₆	3.74	4.05	3.70
Cyclohexane, 1-ethyl-2-methyl-, cis-	C ₉ H ₁₈	3.16	3.26	3.09
1 H-Indene, octahydro-, cis-	C ₉ H ₁₆	0.57	0.76	0.51
Cyclohexane, 1-methyl-2-propyl-	C ₁₀ H ₂₀	1.24	1.16	1.20
Cyclopentane, 1,2-dipropyl-	C ₁₁ H ₂₂	0.27	0.21	0.23
trans-Decalin, 2-methyl-	C ₁₁ H ₂₀	0.75	0.69	0.89
Naphthalene, decahydro-2,6-dimethyl-	C ₁₂ H ₂₂	0.58	0.59	0.60
Cyclohexene, 2-butyl-1,3,3-trimethyl-	C ₁₃ H ₂₄	0.30	0.30	0.32
Polycyclic cycloalkanes (wt %)		4.73	4.56	5.06
1,1'-Bicyclohexyl	C ₁₂ H ₂₂	0.21	0.23	0.24
1,1'-Bicyclohexyl, 2-methyl-, cis-	C ₁₃ H ₂₄	0.93	1.06	1.10
1,1'-Bicyclohexyl, 4,4'-dimethyl-	C ₁₄ H ₂₆	1.05	0.85	1.12
1,1'-Bicyclohexyl, 2-propyl-, cis-	C ₁₅ H ₂₈	2.54	2.42	2.60
Total liquid yield (wt%)		21.77	22.18	22.03
Aviation-range hydrocarbons (%)		70.46	70.24	70.81
Gas				
Carbon monoxide	CO	1.88	1.67	1.81
Methane	CH ₄	9.96	9.89	9.56
Carbon dioxide	CO ₂	1.90	1.91	1.94
Propane	C ₃ H ₈	0.97	1.00	0.92
Total gas yield (wt%)		14.71	14.47	14.23
Char (wt%)		25.29	24.90	25.10
Mass balance (%)		61.77	61.55	61.36

3.3. Reaction mechanism analysis

3.3.1. Evaluation of catalyst hydrodeoxygenation activity

The hydroxyprolysis product of lignin mainly contain two oxygen-containing groups, including hydroxyl group and methoxy group. By removing these oxygen-containing groups, aromatic hydrocarbon can be produced directly from lignin hydroxyprolysis. Cycloalkanes can be further generated by hydrogenation of aromatic hydrocarbon, which is beneficial to increase the calorific value of liquid biofuel. Evaluating the reactivity of catalysts for different C-O functional group removal reactions and benzene ring hydrogenation reactions can help us to design enrichment strategies for specific products.

The methoxy removal rate, hydroxyl removal rate, and benzene ring hydrogenation rate were introduced to evaluate the performance of the catalyst. The methoxy removal rate is the sum of the selectivity of all non-methoxy liquid products. The hydroxyl removal rate is the sum of the selectivity of all non-hydroxyl liquid products. The benzene ring hydrogenation rate is the sum of the selectivity of liquid products with saturated ring structure. The detailed information was shown in [Supporting information](#). The changes of methoxy removal rate, hydroxyl removal rate and benzene ring hydrogenation rate with different reaction conditions corresponding to [Fig. 4](#) and [Fig. 5](#) are shown in [Fig. 6](#).

As shown in [Fig. 6a](#), the increasing order of methoxy removal rate with catalysts was CoMo/SiO₂ (52.35 %) < NiW/SiO₂ (60.41 %) < NiMo/SiO₂ (99.48 %). NiMo/SiO₂ showed the highest methoxy removal rate. With the increase of reaction temperature from 220 °C to 260 °C, the methoxy removal rate increased from 93.92 % to 100 %. The increase of reaction pressure could also promote the removal of methoxy groups. The selectivity of methoxy products was 2.43 % at 1 MPa H₂, but completely disappeared at 2 MPa H₂. Regardless of the reaction time, the methoxy removal rate was close to 100 %. When NiMo/SiO₂ was

used, regardless of the reaction conditions, the methoxy removal rate was greater than 80 %, which indicated that the methoxy removal reaction is easier to occur than the benzene ring hydrogenation reaction and hydroxyl removal reaction.

As shown in [Fig. 6b](#), the increasing order of hydroxyl removal rate with catalysts was CoMo/SiO₂ (42.22 %) < NiW/SiO₂ (50.06 %) < NiMo/SiO₂ (92 %). The combination of Ni and Mo promoted the removal of hydroxyl group. At 220 °C, the removal rate of hydroxyl group was only 13.11 %, resulting in cycloalcohols (80.28 %) and cycloalkanes (12.97 %) dominating the liquid products ([Table S7](#)). The increase of reaction temperature greatly promoted the hydroxyl removal rate, which increased from 13.11 % at 220 °C to 99.76 % at 260 °C. At 260 °C, cycloalkanes (73.78 %) and aromatics (25.99 %) dominated the liquid products. The increase of reaction pressure could also enhance the removal of hydroxyl groups from liquid products. At 1.0 MPa H₂, the hydroxyl removal rate was only 53.22 %. When the hydrogen pressure increased from 1 MPa H₂ to 2 MPa H₂ or 3 MPa H₂, the hydroxyl removal rate was close to 100 %. The increasing order of hydroxyl removal rate with reaction time was 2 h (86.91 %) < 4 h (99.76 %) < 6 h (100 %). The extension of reaction time prolonged the contact time between hydrogen and hydroxy-containing liquid products, which enhanced the removal of hydroxyl groups.

As shown in [Fig. 6c](#), NiMo/SiO₂ (89.89 %) showed a higher benzene ring hydrogenation rate than CoMo/SiO₂ (39.00 %) and NiW/SiO₂ (39.06 %), indicating that the reasonable matching of Ni and Mo greatly promoted the benzene ring hydrogenation ability of the catalyst. The benzene ring hydrogenation rate fluctuated with the increase of reaction temperature. At 220 °C, the liquid products of eugenol catalytic experiments were mainly cycloalcohols (80.28 %) and cycloalkanes (12.97 %), rather than phenolic products (6.62 %) ([Table S7](#)). This indicated that the reactivity of benzene hydrogenation reaction is higher than hydroxyl removal reaction at low reaction temperature. It is interesting to note that the benzene ring hydrogenation rate peaked at 240 °C (89.89 %) and then decreased to 73.83 % at 260 °C, indicating that the benzene ring hydrogenation reaction was no longer dominant. When the reaction temperature was increased from 220 °C to 260 °C, the selectivity of aromatic hydrocarbons increased from 0.13 % to 25.99 %. At 240 °C, the liquid products were mainly cycloalkanes (85.44 %), accompanied by small amounts of aromatic hydrocarbons (6.16 %) and cycloalcohols (7.75 %). When the reaction temperature increased from 240 °C to 260 °C, the yield of aromatic hydrocarbons increased (from 6.16 % to 25.99 %) at the expense of the selectivity of cycloalkanes (from 85.44 % to 73.78 %). The further increase of reaction temperature promoted the formation of aromatic hydrocarbons by dehydrogenation reaction of cycloalkanes, rather than by hydrodeoxygenation of phenolic products. In the catalytic conversion experiment ([Table S8](#)) of ethylcyclohexanol on NiMo/SiO₂, the liquid products were all hydrocarbon products, including aromatic hydrocarbons (3.76 %), unsaturated hydrogenation products (58.57 %) and saturated hydrogenation products (37.67 %). Unsaturated hydrogenation products in liquid products included cyclohexene, 1-ethyl- (39.16 %) and 4-ethylcyclohexene (19.41 %). It can be inferred that the unsaturated hydrogenation products and aromatic hydrocarbons are produced by ethylcyclohexanol with the saturated six-membered ring structure through dehydrogenation reaction. 3.76 % of aromatic hydrocarbons were generated ([Table S8](#)), which further proved the existence of dehydrogenation reaction. At 1 MPa H₂, the liquid products of catalytic experiments of eugenol were mainly aromatic hydrocarbons (37.26 %) and phenolic products (41.30 %), rather than cycloalcohols (5.48 %). This indicated that hydrogen is preferred for hydrodeoxygenation reaction rather than benzene ring hydrogenation reaction under low hydrogen pressure. With the increase of hydrogen pressure, the benzene ring hydrogenation rate increased sharply, from 17.71 % at 1 MPa H₂ to 99.63 % at 3 MPa H₂. At 3 MPa H₂, the main liquid product of the catalytic experiments of eugenol was cycloalkanes (99.31 %), which showed that the increase of hydrogen pressure greatly enhanced the benzene ring hydrogenation

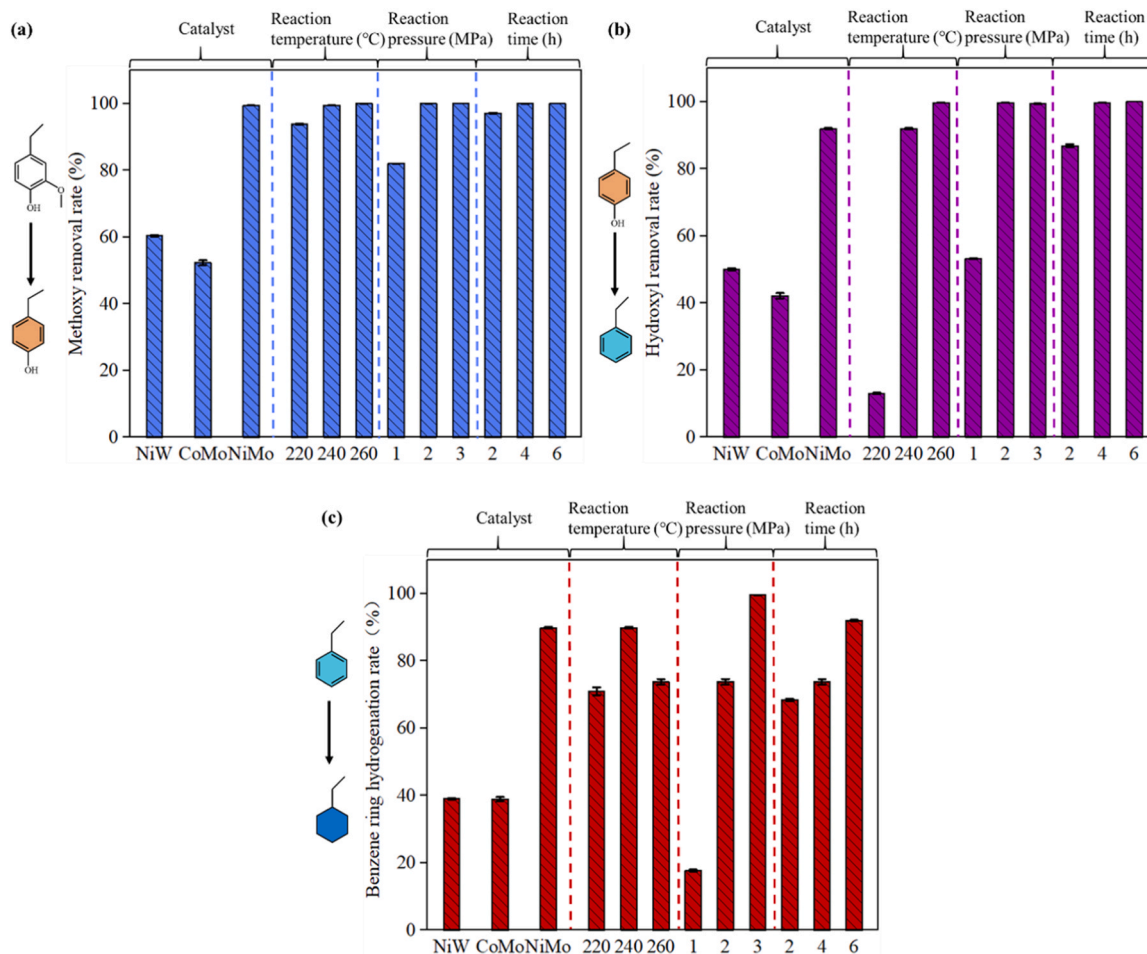


Fig. 6. Variation of methoxy removal rate (a), hydroxyl removal rate (b), and benzene ring hydrogenation rate (c) with the catalyst, reaction temperature, reaction pressure, and reaction time. (10 mmol feedstock, 0.1 g catalyst.).

reaction. The increasing order of benzene ring hydrogenation rate with reaction time was 2 h (68.41 %) < 4 h (73.83 %) < 6 h (92.06 %). At 6 h, the liquid products were mainly cycloalkanes (92.06 %), with small amounts of aromatic hydrocarbons (7.94 %). The increase in reaction time enhanced the benzene ring hydrogenation reaction, thus increasing the selectivity of the cycloalkanes.

3.3.2. Quantum chemical analysis

To clarify the evolution of lignin-derived phenolic compounds into hydrocarbons, the possible reaction pathways were analyzed using quantum chemical calculations. Fig. 7 and Table 3 shows the quantum descriptors of three phenolic modeling compounds, including eugenol, ethylguaiacol, and ethylphenol. BO indicates the bond strength of two adjacent atoms, which can reflect the stability of chemical bonds in a molecule. BO_x represents the maximum bond order of the molecule. The smaller the BO_x , the more unstable the chemical bonds. The Fukui index $f(0)$ reflects the attack ability of free radicals. $f(0)_x$ represents the maximum index of the attack ability of free radicals. The larger the $f(0)_x$, the more easily the molecule is attacked by free radicals [34].

As shown in Table 3, the increasing order of the BO_x index of the three modeling compounds was ethylphenol ($BO_x=1.567$) < ethylguaiacol ($BO_x=1.596$) < eugenol ($BO_x=1.955$). It was inferred that ethylphenol is presumed to have the most unstable structure, followed by ethylguaiacol and finally eugenol. The more unstable the structure, the easier it is to generate the complete reaction product, cycloalkanes, in the catalytic conversion experiment. This was consistent with the decreasing order of the selectivity of cycloalkanes, which was ethylphenol (100 %) > ethylguaiacol (99.1 %) > eugenol (73.83 %). As

shown in Fig. 7, the $BO_{C(1)-O(12)}$ (0.440) was weaker than $BO_{C(6)-O(10)}$ (0.521) in eugenol, which meant that the C(6)–O(10) bond is more easily broken. The hydroxyl and methoxyl positions of ethylguaiacol showed the same trend. This indicated that methoxy is easier to remove than hydroxyl, which is also consistent with experimental results. In terms of ethylphenol, $f(0)-C(1)$ (0.1013e), $f(0)-C(3)$ (0.0966e), $f(0)-C(4)$ (0.0936e), and $f(0)-C(6)$ (0.0891e), were greater than the $f(0)-O(1)$ (0.0865e). Compared with O(11), the radical reactions were more likely to occur on C(1), C(3), C(4), and C(6) that are not connected to oxygen-containing functional groups. It was inferred that in the hydrogen atmosphere, the hydrogen radical is more inclined to attack the four carbons on the benzene ring than the hydroxyl group, which indicated that the benzene ring hydrogenation reaction takes precedence over the hydroxyl removal reaction.

To reveal the influence of Ni species and Mo species of NiMo/SiO₂ on C–O bond breakage, the most stable adsorption configuration, adsorption energy, and dissociation energy of different substrates on Ni(001), MoO₂(001), and MoO₂(001)-O_v were calculated. As shown in Fig. 8 and Table S12, Ni(001) showed strongest adsorption of ethyl guaiacol and phenol with adsorption energy of −3.03 eV and −2.88 eV, respectively. MoO₂(001)-O_v showed the strongest H₂ adsorption (−0.74 eV). It is well known that oxygen vacancy will be generated after MoO₃ is reduced by hydrogen[59]. As shown in Fig. 8d, the presence of oxygen vacancy did enhance the adsorption of MoO₂ for ethyl guaiacol, phenol, and hydrogen. The dissociation energy of different substrates on Ni(001), MoO₂(001), and MoO₂(001)-O_v is revealed in Table S13–14. The dissociation energy of H₂, the methoxy group of ethyl guaiacol, and the hydroxyl group of phenol on Ni(001) were 0.12 eV, 1.62 eV, and 1.57 eV,

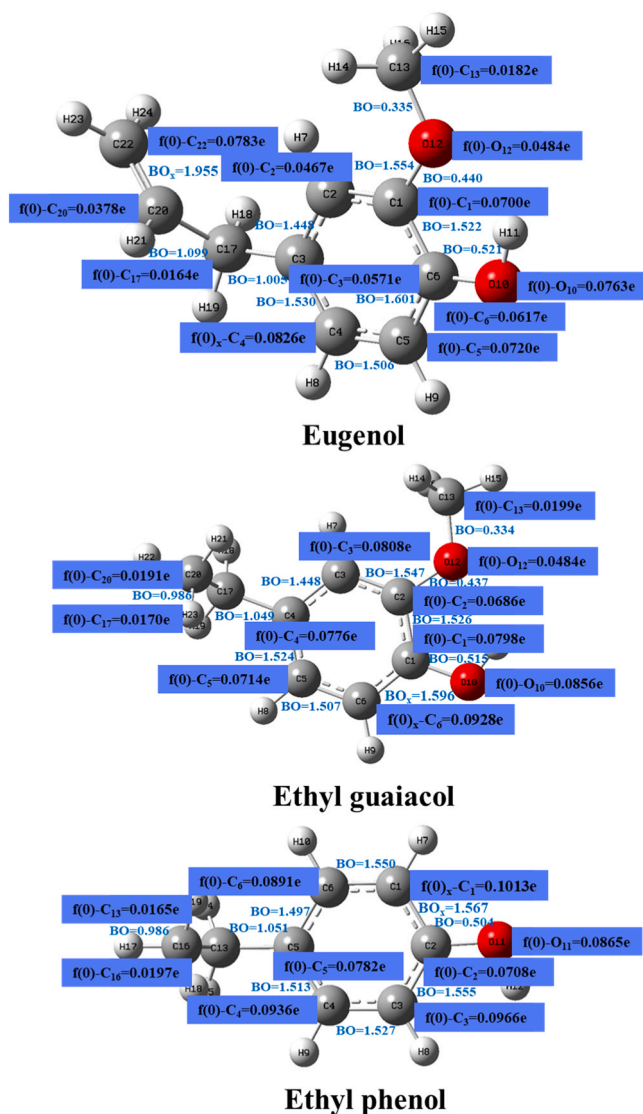


Fig. 7. BO and $f(0)$ indices of eugenol, ethyl guaiacol, and ethyl phenol.

Table 3

The quantum descriptors of the three modeling compounds.

Compounds	Structural formula	Quantum descriptors	
		BO_x	$f(0)_x$
Guaiacol		$C_{20}-C_{22}=1.955$	$C_4=0.0826e$
Ethylguaiacol		$C_1-C_6=1.596$	$C_6=0.0928e$
Ethylphenol		$C_1-C_2=1.567$	$C_1=0.1013e$

respectively. The dissociation energy of the methoxy group of ethyl guaiacol on $MoO_2(001)$ was only 1.20 eV, which suggested that the presence of MoO_2 promotes the dissociation of methoxy groups. The dissociation of H_2 and the C-O bond of phenol were difficult to occur on $MoO_2(001)$ and $MoO_2(001)-O_v$. It is inferred that Ni plays a significant

role in C-O bond breaking of phenol and H_2 dissociation, while MoO_2 enhanced the dissociation of methoxy groups.

Combining experimental and DFT results, the evolution path of ethylguaiacol on the $NiMo/SiO_2$ is summarized in Fig. 9. In this catalytic reaction system, the methoxy group of ethylguaiacol was priority removed through demethoxylation reaction on MoO_2 active site, whose reactivity increased with the increase of reaction pressure and reaction temperature. Then the benzene ring hydrogenation reaction preceded the dehydroxylation reaction, which was proved by Gaussian calculation and experimental results. High pressure hydrogen will promote the benzene ring hydrogenation reaction. With the further increase of temperature and pressure, the dehydroxylation reaction on Ni active site will be enhanced, which led to the formation of cycloalkanes. With the further increase of reaction temperature, the cycloalkane will dehydrogenate to produce aromatic hydrocarbons. This is different from the traditional theory that aromatic hydrocarbons are formed by breaking C-O bond directly by phenols[60]. This interesting phenomenon can make it feasible to regulate the selectivity of cycloalkanes and aromatic hydrocarbons. According to the verification experiment results in Table S5 and Table S6, it was inferred that polycyclic cycloalkanes can be generated through aldol condensation and hydrodeoxygenation reaction of cycloalcohols. The proposed reaction mechanism and reactivity regulation strategy provide guidance for the regulation of aviation biofuel components from lignin catalytic hydrodeoxylation. However, the production of 9.80 wt% CH_4 during lignin catalytic hydrodeoxylation indicated that the branch chain of lignin will inevitably be removed by hydrocracking reaction in the harsh reaction condition. To enrich the aviation biofuels from lignin catalytic hydrodeoxylation and make its application closer to bioeconomy, the development of bimetallic hydrodeoxygenation catalysts with high reactivity under mild reaction conditions still required great efforts.

4. Conclusions

In conclusion, the bimetallic supported on SiO_2 catalysts were synthesized and extensively investigated to determine the evolution path of lignin catalytic hydrodeoxylation. The reasonable matching of Ni and Mo resulted in the highest proportion of Lewis weak and strong acidic sites on $NiMo/SiO_2$ catalyst. All metal active sites were evenly dispersed on the SiO_2 , which may be due to the large specific surface area and plenty of lattice defects of SiO_2 . For $NiMo/SiO_2$, the selectivity of liquid hydrocarbon products and aviation-range hydrocarbons could reach 99.76 % and 99.53 % during eugenol hydrodeoxygenation. For lignin catalytic hydrodeoxylation (2 MPa H_2 , pyrolysis temperature 500 °C, catalytic temperature 300 °C), the average yield of liquid hydrocarbon products was 21.99 wt% with the aviation-range hydrocarbons selectivity of 70.50 %. The scale-up experiment of enzymolysis lignin in continuous flow high pressure fixed bed reactor exhibited a high mass balance (89.66 %).

The increase of reaction pressure and reaction temperature could promote the removal of methoxy groups and hydroxyl groups, which enhanced the formation of liquid hydrocarbon products. There was a positive correlation between hydrogen pressure and benzene ring hydrogenation reactivity. It is worth noting that the dehydrogenation of cycloalkanes was also greatly enhanced, which resulted in the formation of aromatic hydrocarbons at the expense of cycloalkanes. According to the DFT calculation, the methoxy group of phenolic compounds is preferentially dissociated on MoO_2 active site. The hydroxyl group of phenolic compounds is more inclined to dissociate on Ni active site. The methoxy removal reaction was easier to occur than the hydroxyl removal reaction. Benzene ring hydrogenation reaction took precedence over hydroxyl removal reaction. The aromatic hydrocarbons could be generated by the dehydrogenation reaction of cycloalkanes, rather than by hydrodeoxygenation of phenolic products.

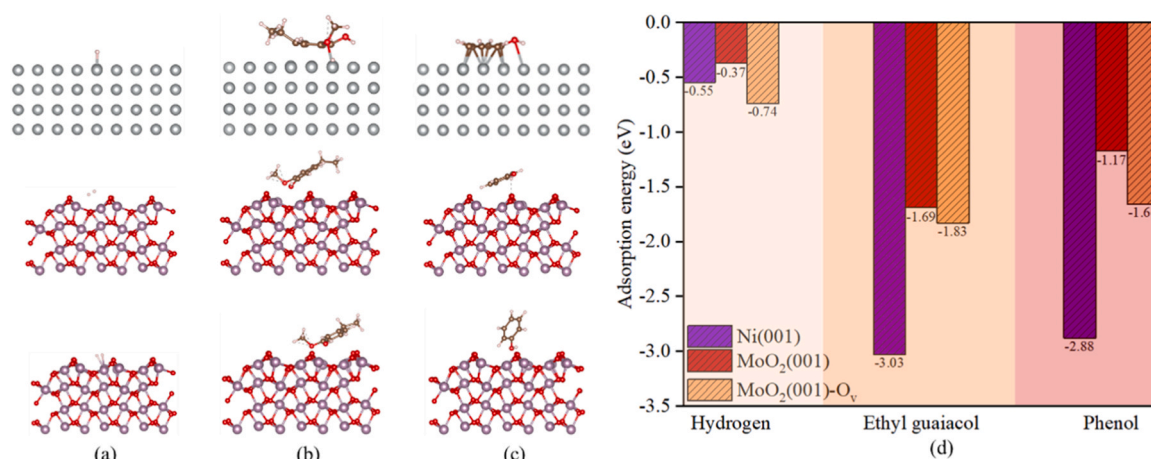


Fig. 8. Front views of the most stable adsorption geometries of H₂ (a), ethyl guaiacol (b), and phenol (c) on Ni(001), MoO₂(001), and MoO₂(001)-O_v, respectively. The brown, pink, red, grey, and purple spheres represent the C, H, O, Ni, and Mo atoms, respectively. (d) The adsorption energies of H₂, ethyl guaiacol, and phenol on Ni(001), MoO₂(001), and MoO₂(001)-O_v.

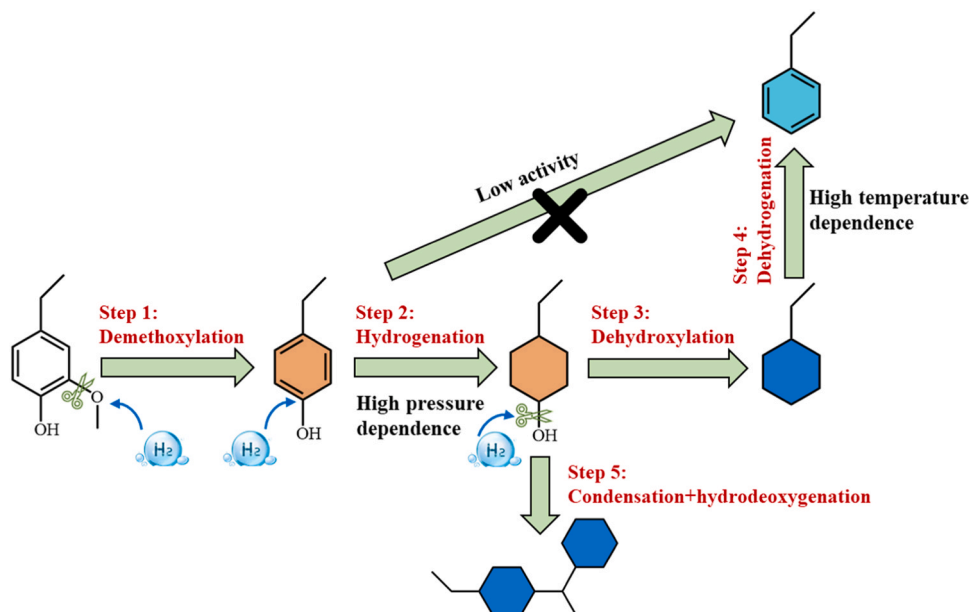


Fig. 9. The evolution path of ethyl guaiacol over the catalysis of NiMo/SiO₂.

CRediT authorship contribution statement

Tan Li: Writing – review & editing, Writing – original draft, Visualization, Validation, Project administration, Methodology, Investigation, Formal analysis, Data curation, Conceptualization. **Bingyan Sun:** Writing – review & editing, Visualization, Data curation, Conceptualization. **Jing Su:** Writing – review & editing, Visualization, Validation, Methodology. **Linjia Yin:** Validation, Software, Formal analysis, Data curation, Conceptualization. **Wanchen Zhu:** Data curation, Resources, Formal analysis. **Kaige Wang:** Writing – review & editing, Writing – original draft, Visualization, Validation, Supervision, Software, Resources, Project administration, Conceptualization. **Yang Meng:** Data curation, Resources, Software, Conceptualization, Formal analysis, Validation.

Declaration of Competing Interest

The authors declare that they have no known competing financial interests or personal relationships that could have appeared to influence

the work reported in this paper.

Data availability

Data will be made available on request.

Acknowledgments

The authors would like to acknowledge financial support from the National Key R&D Program of China (Grant No. 2022YFE0135400), and the National Natural Science Foundation of China (Grant No. 52236011).

Appendix A. Supporting information

Supplementary data associated with this article can be found in the online version at [doi:10.1016/j.apcatb.2024.124092](https://doi.org/10.1016/j.apcatb.2024.124092).

References

- [1] M.L. Stone, M.S. Webber, W.P. Mounfield, D.C. Bell, E. Christensen, A.R.C. Morais, Y. Li, E.M. Anderson, J.S. Heyne, G.T. Beckham, Y. Román-Leshkov, Continuous hydrodeoxygenation of lignin to jet-range aromatic hydrocarbons, *Joule* 6 (2022) 2324–2337.
- [2] U.S. Product Supplied for Crude oil and Petroleum Products. (U.S. Energy Information Administration). https://www.eia.gov/dnav/pet/pet_cons_psup_dc_nus_mbb1.m.htm.
- [3] Short-Term Energy Outlook. (U.S. Energy Information Administration). <https://www.eia.gov/outlooks/steo/>.
- [4] Z. Sun, B. Fridrich, A. de Santi, S. Elangovan, K. Barta, Bright Side of Lignin Depolymerization: Toward New Platform Chemicals, *Chem. Rev.* 118 (2018) 614–678.
- [5] L. Zhang, N. Shang, S. Gao, J. Wang, T. Meng, C. Du, T. Shen, J. Huang, Q. Wu, H. Wang, Y. Qiao, C. Wang, Y. Gao, Z. Wang, Atomically dispersed Co catalyst for efficient hydrodeoxygenation of lignin-derived species and hydrogenation of nitroaromatics, *ACS Catal.* 10 (2020) 8672–8682.
- [6] X. Yue, L. Zhang, L. Sun, S. Gao, W. Gao, X. Cheng, N. Shang, Y. Gao, C. Wang, Highly efficient hydrodeoxygenation of lignin-derivatives over Ni-based catalyst, *Appl. Catal. B: Environ.* 293 (2021).
- [7] S. Li, B. Liu, J. Truong, Z. Luo, P.C. Ford, M.M. Abu-Omar, One-pot hydrodeoxygenation (HDO) of lignin monomers to C9 hydrocarbons co-catalysed by Ru/C and Nb2O5, *Green Chem.* 22 (2020) 7406–7416.
- [8] X. Dou, W. Li, C. Zhu, X. Jiang, Catalytic waste Kraft lignin hydrodeoxygenation to liquid fuels over a hollow Ni-Fe catalyst, *Appl. Catal. B: Environ.* 287 (2021).
- [9] L.F. Sosa, P.M. de Souza, R.A. Rafael, R. Wojcieszak, V. Briois, L.R. Francisco, R. C. Rabelo-Neto, E. Marceau, S. Paul, F.S. Toniolo, F.B. Noronha, Study of the performance of SiO2-supported Mo2C and metal-promoted Mo2C catalysts for the hydrodeoxygenation of m-cresol, *Appl. Catal. B: Environ.* 331 (2023).
- [10] R. Tu, W. Lv, Y. Sun, Y. Wu, X. Fan, E. Jiang, Q. Lu, X. Xu, Ru-RuO2-Nb2O5/H β zeolite catalyst for high-active hydrogenation of lignin derivatives at room temperature, *Chem. Eng. J.* 453 (2023).
- [11] R. Zong, H. Li, W. Ding, H. Huang, Highly dispersed Pd on zeolite/carbon nanocomposites for selective hydrodeoxygenation of biomass-derived molecules under mild conditions, *ACS Sustain. Chem. Eng.* 9 (2021) 9891–9902.
- [12] H. Yang, X. Du, X. Lei, K. Zhou, Y. Tian, D. Li, C. Hu, Unraveling enhanced activity and coke resistance of Pt-based catalyst in bio-aviation fuel refining, *Appl. Energy* 301 (2021).
- [13] Z. Gao, Z. Zhou, M. Wang, N. Shang, W. Gao, X. Cheng, S. Gao, Y. Gao, C. Wang, Highly dispersed Pd anchored on heteropolyacid modified ZrO2 for high efficient hydrodeoxygenation of lignin-derivatives, *Fuel* 334 (2023).
- [14] G. Zaspalov, A. Vutolkina, V. Klimovsky, E. Abramov, V. Vinokurov, A. Glotov, Hydrodeoxygenation of guaiacol over halloysite nanotubes decorated with Ru nanoparticles: effect of alumina acid etching on catalytic behavior and reaction pathways, *Appl. Catal. B: Environ.* (2024) 342.
- [15] R. Insyani, M.-K. Kim, J.-W. Choi, C.-J. Yoo, D. Jin Suh, H. Lee, C. Soo Kim, K. Ho Kim, K. Kim, J.-M. Ha, Selective hydrodeoxygenation of biomass pyrolysis oil and lignin-derived oxygenates to cyclic alcohols using the bimetallic NiFe core-shell supported on TiO2, *Chem. Eng. J.* 446 (2022).
- [16] X. Dou, X. Jiang, W. Li, C. Zhu, Q. Liu, Q. Lu, X. Zheng, H.-M. Chang, H. Jameel, Highly efficient conversion of Kraft lignin into liquid fuels with a Co-Zn-beta zeolite catalyst, *Appl. Catal. B: Environ.* 268 (2020).
- [17] L. He, X. Yin, C. Tao, X. Zhou, Q. Ren, J. Xu, S. Hu, S. Su, Y. Wang, J. Xiang, Self-assembly of CNTs@Ni foam electrode material and its activation effect during catalytic reforming of bio-oil model compound for hydrogen at different temperatures, *Fuel* 336 (2023).
- [18] L. He, X. Yin, C. Tao, X. Zhou, J. Li, Z. Xiong, Y. Tong, S. Hu, S. Su, Y. Wang, J. Xiang, Effects of Different Ni-Fe/Ni foam catalysts on in situ preparation of CNTs@Ni foam electrode materials and H2 during steam reforming of pyrrole, *Energy Fuels* 37 (2023) 7237–7245.
- [19] M. Wang, N. Shang, W. Gao, X. Cheng, S. Gao, C. Wang, Anchoring Co on CeO2 nanoflower as an efficient catalyst for hydrogenolysis of 5-hydroxymethylfurfural, *Fuel* 354 (2023).
- [20] X. Zhang, W. Li, J. Wang, B. Zhang, G. Guo, C. Shen, Y. Jiang, Depolymerization of Kraft lignin into liquid fuels over a WO3 modified acid-base coupled hydrogenation catalyst, *Fuel* 323 (2022).
- [21] H. Duan, J. Dong, X. Gu, Y.K. Peng, W. Chen, T. Issariyakul, W.K. Myers, M.J. Li, N. Yi, A.F.R. Kilpatrick, Y. Wang, X. Zheng, S. Ji, Q. Wang, J. Peng, D. Chen, Y. Li, J.C. Buffet, H. Liu, S.C.E. Tsang, D. O'Hare, Hydrodeoxygenation of water-insoluble bio-oil to alkanes using a highly dispersed Pd-Mo catalyst, *Nat. Commun.* 8 (2017) 591.
- [22] P. He, Q. Yi, H. Geng, Y. Shao, M. Liu, Z. Wu, W. Luo, Y. Liu, V. Valtchev, Boosting the catalytic activity and stability of Ru metal clusters in hydrodeoxygenation of guaiacol through MWW zeolite pore constraints, *ACS Catal.* 12 (2022) 14717–14726.
- [23] H. Zhou, H. Wang, A.D. Sadow, I.I. Slowing, Toward hydrogen economy: Selective guaiacol hydrogenolysis under ambient hydrogen pressure, *Appl. Catal. B-Environ.* (2020) 270.
- [24] C. Wang, L. Guo, K. Wu, X. Li, Y. Huang, Z. Shen, H. Yang, Y. Yang, W. Wang, C. Li, Rational design of Ni-MoO3- catalyst towards efficient hydrodeoxygenation of lignin-derived bio-oil into naphthenes, *J. Energy Chem.* 84 (2023) 122–130.
- [25] F. Yang, M.R. Komarneni, N.J. Libretto, L. Li, W. Zhou, J.T. Miller, Q. Ge, X. Zhu, D. E. Resasco, Elucidating the structure of bimetallic NiW/SiO2 catalysts and its consequences on selective deoxygenation of m-cresol to toluene, *ACS Catal.* 11 (2021) 2935–2948.
- [26] C. Abreu Teles, C. Ciotonea, A. Le Valant, C. Canaff, J. Dhainaut, J.-M. Clacens, F. Bellot Noronha, F. Richard, S. Royer, Optimization of catalyst activity and stability in the m-cresol hydrodeoxygenation through Ni particle size control, *Appl. Catal. B: Environ.* 338 (2023).
- [27] M. Sun, Y. Zhang, W. Liu, X. Zhao, H. Luo, G. Miao, Z. Wang, S. Li, L. Kong, Synergy of metallic Pt and oxygen vacancy sites in Pt-WO3-x catalysts for efficiently promoting vanillin hydrodeoxygenation to methylcyclohexane, *Green Chem.* 24 (2022) 9489–9495.
- [28] Z. Luo, S. Qin, S. Chen, Y. Hui, C. Zhao, Selective conversion of lignin to ethylbenzene, *Green Chem.* 22 (2020) 1842–1850.
- [29] Y. Xue, A. Sharma, J. Huo, W. Qu, X. Bai, Low-pressure two-stage catalytic hydrolysis of lignin and lignin-derived phenolic monomers using zeolite-based bifunctional catalysts, *J. Anal. Appl. Pyrolysis* 146 (2020).
- [30] X. Zhang, W. Tang, Q. Zhang, T. Wang, L. Ma, Hydrodeoxygenation of lignin-derived phenolic compounds to hydrocarbon fuel over supported Ni-based catalysts, *Appl. Energy* 227 (2018) 73–79.
- [31] P.-J. Hsu, J.-W. Jiang, Y.-C. Lin, Does a strong oxophilic promoter enhance direct deoxygenation? A study of NiFe, NiMo, and NiW catalysts in p-cresol conversion, *ACS Sustain. Chem. Eng.* 6 (2017) 660–667.
- [32] W. Kang, H. Lin, S. Yao-Say Solomon Adade, Z. Wang, Q. Ouyang, Q. Chen, Advanced sensing of volatile organic compounds in the fermentation of kombucha tea extract enabled by nano-colorimetric sensor array based on density functional theory, *Food Chem.* 405 (2023).
- [33] Y. He, Y. Zhao, M. Chai, Z. Zhou, M. Sarker, C. Li, R. Liu, J. Cai, X. Liu, Comparative study of fast pyrolysis, hydrolysis and catalytic hydrolysis of poplar sawdust and rice husk in a modified Py-GC/MS microreactor system: Insights into product distribution, quantum description and reaction mechanism, *Renew. Sustain. Energy Rev.* (2020) 119.
- [34] F. Miao, Z. Luo, Q. Zhou, L. Du, W. Zhu, K. Wang, J. Zhou, Study on the reaction mechanism of C8+ aliphatic hydrocarbons obtained directly from biomass by hydrolysis vapor upgrading, *Chem. Eng. J.* 464 (2023).
- [35] Q. Cai, T. Gong, T. Yu, S. Zhang, Comparison of hydrocracking and cracking of pyrolytic lignin over different Ni-based catalysts for light aromatics production, *Fuel Process. Technol.* 240 (2023).
- [36] M.A. Salam, Y.W. Cheah, P.H. Ho, L. Olsson, D. Creaser, Hydrotreatment of lignin dimers over NiMoS-USY: effect of silica/alumina ratio, *Sustain. Energy Fuels* 5 (2021) 3445–3457.
- [37] F. Huang, P.M. Singh, A.J. Ragauskas, Characterization of milled wood lignin (MWL) in Loblolly pine stem wood, residue, and bark, *J. Agric. Food Chem.* 59 (2011) 12910–12916.
- [38] H. Wang, T. Li, J. Su, K. Miao, K. Wang, Noncatalytic hydrolysis of lignin in a high pressure micro-pyrolyzer, *Fuel Process. Technol.* 233 (2022).
- [39] T. Li, K. Miao, Z. Zhao, Y. Li, H. Wang, A. Watanabe, N. Teramae, K. Wang, Understanding cellulose pyrolysis under hydrogen atmosphere, *Energy Convers. Manag.* 254 (2022).
- [40] T. Li, J. Su, C. Wang, A. Watanabe, N. Teramae, H. Ohtani, K. Wang, Advances in the development and application of analytical pyrolysis in biomass research: a review, *Energy Convers. Manag.* (2022) 271.
- [41] G.W.T.M.J. Frisch, H.B. Schlegel, G.E. Scuseria, M.A. Robb, J.R. Cheeseman, J.A. Montgomery, Jr. T., Vreven, K.N., Kudin, J.M., Burant, J.M. Millam, S.S., Iyengar, J., Tomasi, V., Barone, B., Mennucci, M., Cossi, G., Scalmani, N., Rega, G.A., Petersson, H., Nakatsuji, M., Hada, M., Ehara, K., Toyota, R. Fukuda, J., Hasegawa, M., Ishida, T., Nakajima, Y., Honda, O., Kitao, H., Nakai, M. Klene, X., Li, J.E., Knox, H.P., Hratchian, J.B., Cross, V., Bakken, C., Adamo, J. Jaramillo, R., Gomperts, R.E., Stratmann, O., Yazyev, A.J., Austin, R., Cammi, C. Pomelli, J.W., Ochterski, P.Y., Ayala, K., Morokuma, G.A., Voth, P., Salvador, J.J. Dannenberg, V. G., Zakrzewski, S., Dapprich, A.D., Daniels, M.C., Strain, O. Farkas, D.K., Malick, A. D., Rabuck, K., Raghavachari, J.B., Foresman, J.V., Ortiz, Q. Cui, A.G., Baboul, S., Clifford, J., Cioslowski, B.B., Stefanov, G., Liu, A. Liashenko, P., Piskorz, I., Komaromi, R.L., Martin, D.J., Fox, T., Keith, M.A., Al-Laham, C.Y., Peng, A., Nanayakkara, M., Challacombe, P.M.W., Gill, B., Johnson, W., Chen, M.W., Wong, C.Gonzalez, and J.A. Pople, Gaussian 03, Revision C.02, Wallingford, CT, 2004.
- [42] T. Lu, F. Chen, Multiwfn: a multifunctional wavefunction analyzer, *J. Comput. Chem.* 33 (2012) 580–592.
- [43] G. Kresse, Ab-initio molecular-dynamics for liquid-metals, *J. Non-Cryst. Solids* 193 (1995) 222–229.
- [44] G. Kresse, J. Furthmuller, Efficiency of ab-initio total energy calculations for metals and semiconductors using a plane-wave basis set, *Comput. Mater. Sci.* 6 (1996) 15–50.
- [45] T. Nishitoba, K. Matsumoto, Y. Ishizaka, N. Arai, K. Takeuchi, N. Fukaya, T. Fujitani, A. Endo, H. Yasuda, K. Sato, J.C. Choi, Controlled growth of platinum nanoparticles on amorphous silica from grafted Pt-disilicate complexes, *ACS Omega* 7 (2022) 47120–47128.
- [46] Z. Zhao, Z. Li, X. Zhang, T. Li, Y. Li, X. Chen, K. Wang, Catalytic hydrogenolysis of plastic to liquid hydrocarbons over a nickel-based catalyst, *Environ. Pollut.* (2022).
- [47] T. Liu, P. Sun, H. Zhu, T. Yang, B. Tang, C. Peng, The effect of hydroxyl and metal synergetic structures on the FCC diesel hydrotreating performance of NiMo/Al2O3 catalysts, *Fuel* 356 (2024).
- [48] G. Zhou, H. Liu, Y. Xing, S. Xu, H. Xie, K. Xiong, CO2 hydrogenation to methane over mesoporous Co/SiO2 catalysts: effect of structure, *J. CO2 Util.* 26 (2018) 221–229.
- [49] Q. Cui, S. Wang, Q. Wei, L. Mu, G. Yu, T. Zhang, Y. Zhou, Synthesis and characterization of Zr incorporated small crystal size Y zeolite supported NiW catalysts for hydrocracking of vacuum gas oil, *Fuel* 237 (2019) 597–605.

- [50] X. Li, X.I. Pereira-Hernandez, Y. Chen, J. Xu, J. Zhao, C.-W. Pao, C.-Y. Fang, J. Zeng, Y. Wang, B.C. Gates, J. Liu, Functional CeOx nanoglues for robust atomically dispersed catalysts, *Nature* 611 (2022) 284.
- [51] A. Saraeian, S.J. Burkhov, D.P. Jing, E.A. Smith, B.H. Shanks, Catalyst property effects on product distribution during the hydrodeoxygenation of lignin pyrolysis vapors over MoO₃/γ-Al₂O₃, *Acs Sustain. Chem. Eng.* 9 (2021) 6685–6696.
- [52] J. Weber, A. Thompson, J. Wilmoth, V.S. Batra, N. Janulaitis, J.R. Kastner, Effect of metal oxide redox state in red mud catalysts on ketonization of fast pyrolysis oil derived oxygenates, *Appl. Catal. B-Environ.* 241 (2019) 430–441.
- [53] B. Chen, C.Z. He, M.F. Cao, X.Q. Qiu, X.P. Ouyang, Y. Qian, Fabricating nickel phyllosilicate-like nanosheets to prepare a defect-rich catalyst for the one-pot conversion of lignin into hydrocarbons under mild conditions, *Green Chem.* 24 (2022) 846–857.
- [54] P. Koley, S.C. Shit, Y.M. Sabri, B.S. Rao, L. Nakka, J. Tardio, J. Mondal, Looking into more eyes combining in situ spectroscopy in catalytic biofuel upgradation with composition-graded Ag-Co core-shell nanoalloys, *Acs Sustain. Chem. Eng.* 9 (2021) 3750–3767.
- [55] X.Y. Li, Q. Wang, J.L. Chen, S.R. Li, D.C. Wang, Z.F. Zheng, One-step hydrotreatment of inedible oil for production the second-generation biofuel over Pt-Sn/SAPO-11 catalyst, *J. Anal. Appl. Pyrolysis* 156 (2021).
- [56] T. Li, J. Su, H. Wang, C. Wang, W. Xie, K. Wang, Catalytic hydropyrolysis of lignin using NiMo-doped catalysts: Catalyst evaluation and mechanism analysis, *Appl. Energy* (2022) 316.
- [57] T. Li, J. Su, L. Yin, X. Zhang, C. Wang, X. Li, J. Zhang, K. Wang, The synergistic effect of CuO and Cu⁺ for one-step synthesis of aviation biofuel from biomass-derived ketones, *Green. Chem.* (2023).
- [58] J. Zhang, N. Zheng, J. Wang, Comparative investigation of rice husk, thermoplastic bituminous coal and their blends in production of value-added gaseous and liquid products during hydropyrolysis/co-hydropyrolysis, *Bioresour. Technol.* 268 (2018) 445–453.
- [59] K. Murugappan, E.M. Anderson, D. Teschner, T.E. Jones, K. Skorupska, Y. Román-Leshkov, Operando NAP-XPS unveils differences in MoO₃ and Mo₂C during hydrodeoxygenation, *Nat. Catal.* 1 (2018) 960–967.
- [60] B. Zhang, B.K. Biswal, J. Zhang, R. Balasubramanian, Hydrothermal treatment of biomass feedstocks for sustainable production of chemicals, fuels, and materials: progress and perspectives, *Chem. Rev.* (2023).